Disponible en **www.hormigonyacero.com**
Hormigón y Acero 2024
https://doi.org/10.33586/hya.2022.3088

# Time-Variation of Shear Forces Affecting the Impact Resistance of Reinforced Concrete Beams

## *Influencia de la variación temporal de la ley de esfuerzos cortantes en a resistencia frente a impacto de vigas de hormigón armado*

**Gonzalo S.D. Ulzurrun[a], Carlos Zanuy[a,*]**

[a] *Department of Continuum Mechanics and Structures, ETS Ingenieros de Caminos, Canales y Puertos, Universidad Politécnica de Madrid, Spain*

**Recibido el 14 de julio de 2022; revisado el 13 de octubre de 2022, aceptado el 18 de noviembre de 2022**

ABSTRACT

One of the most hazardous scenarios for reinforced concrete (RC) members is due to the actuation of impact loads. Such impacts may be either accidental or induced events. Experimental research has demonstrated that the failure mode of RC beams is strongly governed by shear, due either to the formation of a shear plug close to the impact point or to the full development of inclined shear-bending cracks along the shear span. In order to analyze the shear strength under impact conditions, it is essential to understand how the development of inertia forces leads to a time-dependent distribution of shear forces and bending moments which differs significantly to those produced by quasi-static loads. In the paper, an experimentally-based determination of shear forces and follow-up of crack pattern is presented for RC beams tested under impact loads. Sectional forces' distributions are determined experimentally by measuring all the necessary terms involved in the dynamic equilibrium of forces: support reactions, impact force and inertia forces. While dynamic load cells have been employed to capture reactions and impact force, a Digital Image Correlation (DIC) technique supported by a high-speed camera has been used to obtain inertia forces from the accelerations derived from the displacement field in dynamic regime. Thereby, the evolution of shear forces at critical sections can be understood and the ultimate shear strength can be discussed with the help of M-V interaction diagrams..

KEYWORDS: shear strength; impact; experimental analysis; reinforced concrete.



RESUMEN

Uno de los escenarios más críticos para los elementos de hormigón armado es el debido a la actuación de cargas de impacto. Tales acciones pueden ocurrir de forma accidental o inducida. La evidencia experimental ha demostrado que el modo de fallo frente a impacto de vigas de HA está fuertemente gobernado por el cortante, bien por la formación de un cono de cortante en la zona del impacto o por el desarrollo completo de fisuras de cortante-flexión a lo largo del vano. Para analizar la resistencia a cortante bajo impacto, es esencial entender cómo la aparición de fuerzas de inercia produce leyes de esfuerzos variables con el tiempo durante el evento del impacto, con distribuciones diferentes a las que se forman bajo cargas cuasi-estáticas. En el presente artículo, se presenta una metodología experimental para la determinación de las leyes de esfuerzos y el seguimiento del mapa de fisuras en vigas de HA durante ensayos de impacto. Las leyes de esfuerzos se determinan experimentalmente midiendo todos los términos que influyen en las ecuaciones de equilibrio: reacciones en los apoyos, fuerza del impacto y fuerzas de inercia. Se emplean células de carga dinámicas para la medición de reacciones y fuerza de impacto, mientras que las aceleraciones causantes de las fuerzas de inercia se obtienen a partir del campo de desplazamientos completo que se captura mediante la técnica de correlación digital de imagen apoyada por una cámara de alta velocidad de grabación. De esta manera, se puede entender la evolución de los esfuerzos cortantes en las secciones críticas, y la resistencia a cortante se puede analizar con diagramas de interacción cortante-momento en régimen dinámico.

PALABRAS CLAVE: resistencia a cortante; impacto; análisis experimental; hormigón armado.



* Persona de contacto / *Corresponding author*:
Correo-e / *e-mail*: carlos.zanuy@upm.es (Carlos Zanuy)

How to cite this article: Ulzurrun, G.S.D, & Zanuy, C. (2022) Time-Variation of Shear Forces Affecting the Impact Resistance of Reinforced Concrete Beams, *Hormigón y Acero* 75(302-303):65-78, https://doi.org/10.33586/hya.2022.3088

### Notation

| | |
|---|---|
| $F$ | impact force |
| $L$ | beam length |
| $L_1$ | beam end cantilever length |
| $M$ | bending moment |
| $V$ | shear force |
| $R$ | reaction force |
| $a$ | acceleration |
| $b$ | section width |
| $d$ | section effective depth |
| $f_c$ | compressive strength of concrete |
| $f_{ct}$ | tensile strength of concrete |
| $f_y$ | yield strength of steel |

| | |
|---|---|
| $h$ | section height |
| $i$ | inertia force |
| $m$ | mass per unit length |
| $s$ | horizontal coordinate |
| $t$ | time |
| $v$ | vertical displacement |
| $x$ | horizontal coordinate from the beam end |
| $\Delta t$ | time step size |
| $\Phi$ | diameter of steel bars |
| $\rho$, $\rho_w$ | longitudinal and shear steel reinforcing ratio |

*ACRONYMS*

| | |
|---|---|
| **DIC** | Digital image correlation |
| **DIF** | Dynamic increase factors |
| **fps** | Frame per second |
| **HSV** | High-speed video |
| **LVDT** | Linear variable differential transformer |
| **MCFT** | Modified Compression Field Theory |
| **RC** | Reinforced concrete |
| **SMCFT** | Simplified Modified Compression Field Theory |
| **UPM** | Technical University of Madrid |

## 1. INTRODUCTION

Experimental techniques in the field of structural engineering research have experienced a significant advance for the last years as a result of the combination of technological development and reduction of costs. Nowadays, photogrammetric full-field experimental methods (digital image correlation, laser) or distributed fiber sensors (optic, Bragg) allow for a wide follow-up of deformations without the necessity of using local sensors like strain gauges, LVDTs or accelerometers [1-5]. A further advantage of full-field techniques arises in case of extreme loading tests (impacts or explosions), where the violent nature of the load event can produce severe damage or even breakage of the sensors. In fact, impact load testing is one of the most complex experimental configurations due to the extremely short duration (of the order of few milliseconds), the consequent fast time-dependent kinematics and the difficulties associated with taking measurements. In turn, experimental evidence on the impact performance of concrete structures is a need due to the lack of understanding of the interaction of structural phenomena.

Shear strength of reinforced concrete elements, especially for those without shear reinforcement, has been a persistent research issue since the collapse of a warehouse of the US air force in Ohio [6]. Even though plenty of shear strength models have been presented so far (e.g. [7-9]), lively discussions are still usual in standardization committees and different approaches can be found in the design codes [10-13]. For the last decade, the Structural Engineering Group of the Technical University of Madrid (UPM) has paid attention at the shear strength of reinforced concrete beams without stirrups under extreme loading scenarios, like high-cycle fatigue [14-17] or impact loading [18,19]. Regarding impact events, they are one of the most hazardous scenarios for reinforced concrete structures, which may be due to either accidental (e.g. rockfalls, collisions) or induced (e.g. terrorist attacks) sources.

Experimental research has demonstrated that the impact failure mode of reinforced concrete beams is strongly governed by shear, without regard of the fact that the beams might be designed to fail by flexure under quasi-static loading [20,21]. Such a change of the failure type from flexure (quasi-static) to shear (impact) can be explained by the interaction of the following mechanisms: modification of the material properties of concrete and steel due to strain-rate effects, severe local damage produced at the impacted zone, and development of inertia forces. Due to the former effects, the pattern of shear failure under impact can present both the formation of a shear plug close to the impact point and diagonal cracks running from the impact point to the supports [22,23]. In order to gain understanding of the shear failure mode and the mobilized resisting mechanisms under impact, it is essential to understand how the development of inertia forces leads to a time-dependent distribution of shear forces and bending moments which differs from those produced by quasi-static loads.

Recent research has shown that the impact response of a reinforced concrete beam can be divided in two stages: a first impulsive one in which the beam responds locally developing very high inertia forces at the impacted region, and a subsequent stage in which the global behaviour of the beam is activated. Both experimental observation [22] and nonlinear dynamic finite element analyses [23] have confirmed that the shear-plug failure occurs during the first stage, when the real span length of the beam has little influence and the beam works with a reduced effective span length [24-26]. In addition, the formation of longer diagonal shear cracks takes place during the global stage response in a shear-bending interaction mechanism, accompanied with the opening of flexural cracks and widening of existing ones. It must be stated that the relevant role played by inertia forces in the distribution of sectional forces and the induced shear failure development has been mainly recognized in the last years. Previously, the differences between quasi-static and impact responses were mainly attributed to strain-rate effects. That is why even advanced design codes include formulations of so-called dynamic increase factors (DIF) which provide the strain-rate influence on the material properties [12,27]. Nowadays, the influence of strain-rate is demonstrated to be moderate in low to medium-velocity impact tests where the mobilized strain rate is within the range of 1-10 s-1 [19,28]. Therefore, the dynamic evolution of sectional forces is critical to understand the RC sensitivity to brittle failure nodes in the impact range.

In the present paper, an experimental campaign on reinforced concrete beams with and without shear reinforcement is presented in order to investigate experimentally on the determination of sectional forces in medium-velocity drop-weight tests. In addition to impact experiments, quasi-static reference tests have been completed in companion specimens in order to compare the quasi-static and the impact response. The research has made use of the instrumented drop-weight testing machine of the Structural Engineering Group at UPM, which is complemented with a high-speed video (HSV) camera. An experimental technique is present-

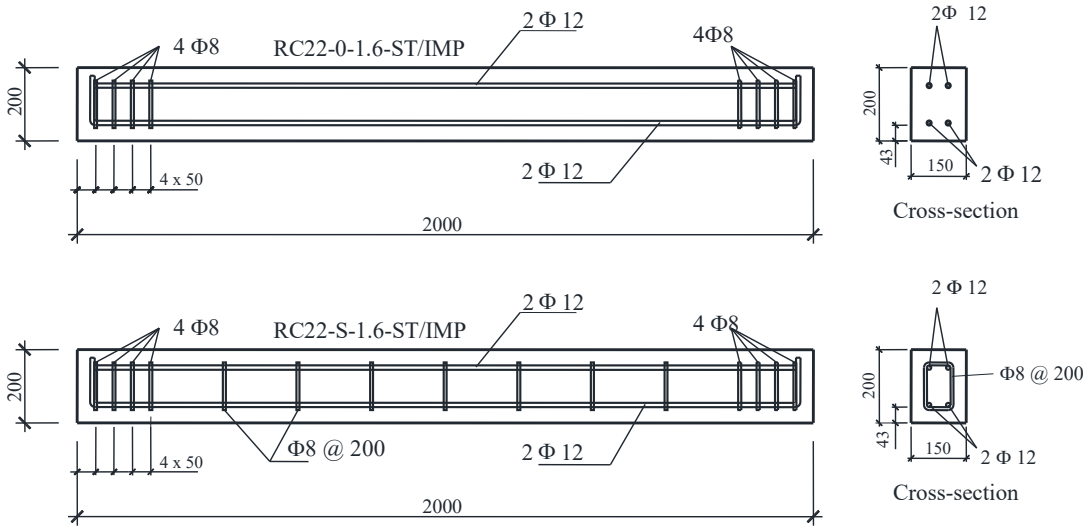


Figure 1. Geometry and reinforcement layout of beam specimens. Dimensions in mm. Note: the clear cover of 43 mm is to the edge of the main longitudinal reinforcement.

ed, which takes advantage of the combined use of dynamic load cells (measurement of reaction and impact forces) and HSV-supported DIC (determination of the time-dependent distribution of inertia forces from the accelerations derived from the displacement field), so that all the components of the dynamic equilibrium can be captured and verified. Therefore, the evolution of the distribution of sectional forces (bending moments and shear forces) can be estimated from the experimental determination of all terms involved in the dynamic equilibrium of motion

## 2. EXPERIMENTAL RESEARCH

### *2.1. Description of specimens*

The experimental campaign included a series of four reinforced concrete beams, among which two were tested under quasi-static loading and the other two were subjected to a drop weight impact at the midspan. The list of specimens and test types is detailed in Table 1. The geometry of the specimens and the details of the reinforcement can be found in Figure 1. As it can be observed, the only difference between the beam specimens was the presence of shear reinforcement (in specimens RC22-S-1.6-ST and RC22-S-1.6-IMP) or not (in specimens RC22-0-1.6-ST and RC22-0-1.6-IMP). The beams had a rectangular cross-section of 150 x 200 mm and total length (L) of 2000 mm. The longitudinal reinforcement consisted of 2 bars of 12 mm diameter of B500 SD steel (characteristic yield and ultimate strength of 500 and 575 MPa, respectively [11,29]) at the bottom and the top of the beams. Thus, the steel reinforcing ratio was $\rho$ = 1.0 %, which ensures that yielding of the longitudinal reinforcement is reached before shear failure under quasi-static loading according to common design rules [11], even for the beams without shear reinforcement (RC22-0-1.6-ST and RC22-0-1.6-IMP). The shear reinforcement of specimens RC22-S-1.6-ST and RC22-S-1.6-IMP consisted of stirrups of 8 mm diameter spaced 200 mm ($\rho_w$ = 0.3 %). The fresh concrete was provided by a local ready-mix supplier and the beams were casted in the laboratory. The concrete mix included 330 kg/m³ of cement CEM II/A-L 42.5R, with a water/cement ratio of 0.46 and maximum aggregate size of 12 mm. The average compressive and indirect tensile strength at 28 days were 26.6 MPa (CoV = 0.08) and 2.5 MPa (CoV = 0.04), respectively (measured on three 150 x 300 mm cylinders each).

TABLE 1.
**List of tests**

| Specimen ID | Test type | Stirrups | Span (m) | Longitudinal reinforcement ratio $\rho$(%) | Shear reinforcement ratio $\rho_w$(%) |
|---|---|---|---|---|---|
| RC22-0-1.6-ST | Quasi-static | No | 1.60 | 1.0 | 0.0 |
| RC22-0-1.6-IMP | Impact | No | 1.60 | 1.0 | 0.0 |
| RC22-S-1.6-ST | Quasi-static | Yes | 1.60 | 1.0 | 0.3 |
| RC22-S-1.6-IMP | Impact | Yes | 1.60 | 1.0 | 0.3 |

### *2.2. Testing configuration*

The specimens were tested with a three-point bending configuration with a span length of 1.6 m between supports, both in the quasi-static and impact tests. In case of quasi-static tests, the load was applied at the midspan with a hydraulic actuator under displacement control at a rate of 0.01 mm/s. The applied load and the midspan deflection were measured with a load cell and an LVDT at a sampling rate of 5 Hz.

The impact tests were performed with the instrumented drop-weight testing machine of the Structural Engineering Group at UPM [18,30]. Drop-weight testing has revealed as a powerful way to understand the failure mechanisms in impact tests (a comprehensive review on the utilization of drop-weight machines has been reported by [31]). The employed facility includes dynamic load cells at the supports

and the striking end of the impact hammer which allow capturing the reactions and impact force during the tests. A sampling rate of 40 kHz was used. In addition, two accelerometers of ±1000g range were attached at the centre of the midspan section of the specimens and at the falling weight (Figure 2a). The specimens were placed simply supported (yoked to avoid uplifting) with a span length of 1.6 m and they were subjected to an impact at the midspan caused by a mass of 100 kg dropped from a height of 1.8 m (Figure 2). The impactor consists of a stiff guided mass carriage (variable between 100 and 200 kg) with a hammer tup. The supports and the impactor hammer ends are metallic cylinders with a radius of 29 mm and a width of 160 mm. The contact between these cylinders and the RC beam is direct, without any intermediate plates. After the first impact, the impactor eventually rebounds and hits again the specimens, but much later than the first impact, wherby the effects of subsequent impacts is not dealt with in the present paper.

In order to capture the total response of tested specimens, a high-speed and high-resolution video camera FASTCAM NOVA S9 by Photron was used to record the impact tests (Figure 2c). Due to the impulsive nature of impact tests, a high recording rate is more than convenient, especially to capture the first stage of local response and eventual shear-plug formation. In the present campaign, videos of 12-bit images were captured at a rate of 22 500 fps with a shutter speed of 1/50 ms and a resolution of 1024×288 px. The camera was equipped with a lens Nikkon AF-S 20mm F/1.8G ED with a fixed focal length of 20 mm. The recorded area of the beam (Figure 2b) is a frame of 1680 × 472.5 mm, which covers the area between supports and twice the depth of the beam. Thus, the px/mm equivalence has been 1 px = 1.64 mm. The speckle pattern was painted on one of the sides of the specimens. Two speckle patterns were employed, consisting of randomly painted black points of 18 and 25 mm average size on white background, for the beam with and without stirrups, respectively. These sizes were defined to reduce the influence of the distortion due to beam movement during the exposure time of each frame. Likewise, the head of the impacting mass had a speckle pattern with smaller black points (average size of 10 mm), according to the available space. Thus, the projectile displacements and the deformed shape of the specimens can be analyzed with DIC technique. GOM Correlate software [32] was used in the present research for the post-processing of the images. Some authors [33-35] have discussed on how to define the facet mesh and post-processing key parameters for an appropriate DIC analysis of impact tests. In the present research, the facet size employed to obtain punctual displacements is 20 and 40 px (32.8 and 65.6 mm) for the falling mass and beam, respectively. These formed a grid of 3 × 25 points on the beam, Figure 2(b). In addition, some of the points were employed as reference to define digital extensometers just in the locations where shear cracks developed. As full-field strain diagrams are a useful method to assess the crack development with the help of DIC [33], a triangular mesh with a facet size of 20 px and a distance between mesh points of 9 px (14.76 mm) was employed to understand the crack evolution. In addition, it is possible to obtain other parameters (such as strains) by post-processing the mesh displacements.

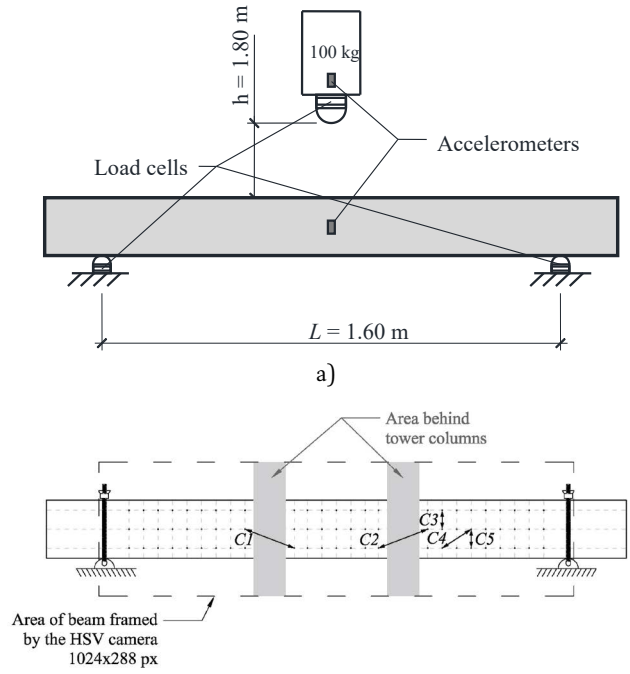


c)

Figure 2. Configuration of impact tests: (a) sensors and test setup, (b) DIC measurement grid and digital extensometers, (c) view of the testing facility.

### *2.3. Experimental derivation of sectional forces*

DIC supported with HSV has the advantage that the full-field response of tested specimens can be captured [36-38], in contrast with the large number of sensors that would be required for a detailed definition of the structural response by means of accelerometers, LVDTs or similar. Moreover, such sensors can be eventually damaged due to the severity of the impact events. With respect to previous research, where the sampling rate has been of up to 5000 fps [28,33,39], the present experimental campaign has been analyzed with a sampling rate 4.5 times higher in order to fully capture both the local and global response of the specimens. In addition, the combination of HSV-based DIC with load-cell measurements (reactions and impact force) allows for a complete experimental determination of the components of the dynamic equation of motion, as detailed in the following paragraphs. The capture of the progressive propagation of concrete

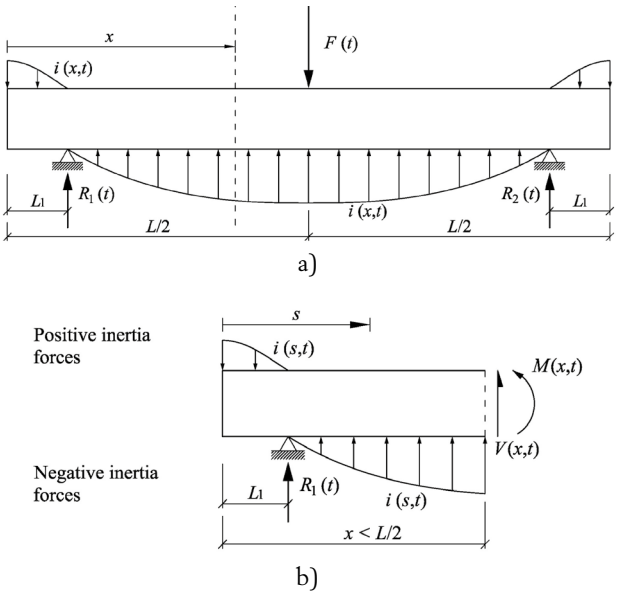


Figure 3. Dynamic equilibrium: (a) global equilibrium of forces and (b) determination of sectional forces.

cracks can be also correlated with such measurements and DIC results.

In an impact test of a simply supported beam, the determination of sectional forces (shear forces and bending moments) is affected by the development of inertia forces ($i(x,t)$), which balance the difference between the reactions ($R_1(t)$ and $R_2(t)$) and the impact force ($F(t)$), as follows (Figure 3(a)):

$$F(t) = \int_{x=0}^{x=L} i(x,t)\, dx = R_1(t) + R_2(t) \tag{1}$$

where the damping force is neglected (if a 2% damping ratio is assumed, the total damping force component is around 80 times smaller than the impact force). Sectional forces are variable with time. From local equilibrium (Figure 3(b)), the sectional forces at any cross-section at a distance $x$ from the left end can be calculated as (the contribution of the rotational inertia force to the equilibrium of moments can be neglected):

$$V(x,t) = -R_1(t) + \int_{s=0}^{s=x} i(s,t)\, ds,\ L_1 < x < L/2 \tag{2}$$

$$M(x,t) = (x - L_1)\, R_1(t) - \int_{s=0}^{s=x} (x-s)\, i(s,t)\, ds,\ L_1 < x < L/2 \tag{3}$$

In the previous equations, the value of the reactions $R_1(t)$ and $R_2(t)$ can be experimentally obtained with the load cells, while the distribution of inertia forces can be derived from the accelerations based on the DIC. Note that the hammer impact force $F(t)$ is not necessary for the estimation of sectional forces in the present simply supported beams, but it is useful for double-check verifications and refinement of the method to derive sectional forces (refer to Section 3.3). The distribution of inertia forces is as follows:

$$i(x,t) = -m(x)\, a(x,t) \tag{4}$$

where $m(x)$ is the mass per unit length of the beam and $a(x,t)$ is the upwards distribution of accelerations. With the help of the DIC, the accelerations are calculated numerically by double derivation of the vertical displacement field:

$$a_i(t) = \frac{v_i(x+\Delta t) - 2v_i(t) + v_i(t+\Delta t)}{\Delta t^2} \tag{5}$$

where $\Delta t$ is the time between two photographs (here, $\Delta t$ = 0.044 ms).

The response of the specimen was recorded with a grid of 3×25 facet points between the supports. Those were distributed with a spacing of 50 and 65 mm in the longitudinal and vertical direction, respectively. The longitudinal grid was adapted to avoid the areas of the specimens hidden by the columns of the testing facility and the steel yokes at the supports (Figure 2b). Vertically, the three points of the grid have been distributed at the section center and near the top and bottom faces. Measurements in areas not recorded by HSV camera, including the short cantilevers at beams ends ($L_1$), were obtained by data extrapolation.

In order to limit the influence of eventual measurement noise in the derivation of accelerations, data treatment working as spatial and time filters has been used. Two ways of spatial filters were employed. One consisted in the above explained estimation of displacements from the three facet points at each cross-section. The other spatial filter consisted on averaging the distribution of sectional forces at the two specimens' halves considering the symmetric and anti-symmetric distribution of bending moments and shear forces, respectively. Regarding measurements along time, a centered moving-average filter was employed for accelerations using a five-step window.

## 3. EXPERIMENTAL RESULTS

### *3.1. Reference quasi-static response*

The load-midspan deflection diagrams of the beams tested under quasi-static loading are presented in Figure 4, and the crack patterns after testing are given in Figure 5(a) and (b). In the two tests, a very similar value of the peak load was obtained, which corresponded to yielding of the bottom tensile reinforcement at the midspan (even a slightly higher load was obtained for the specimen without stirrups). Before peak load, typical development of flexural cracks was observed from the bottom face towards the compression zone at midspan, with some inclination of the cracks formed further from the load application point. Soon after peak load, the beam without shear reinforcement developed a wide shear crack which produced a large release of the carrying capacity. In contrast, the beam with shear reinforcement was able to keep deforming with a very smooth decrease of the carrying load due to progressive crushing of the compression zone at midspan (some hairline shear cracks also opened but the stirrups did not allow their widening).

According to the evidence from the reference quasi-static tests, the presence of shear reinforcement was responsible to allow for a ductile post-yielding response, even though the same pre-peak response with yielding of longitudinal steel was attained by the beam without stirrups.

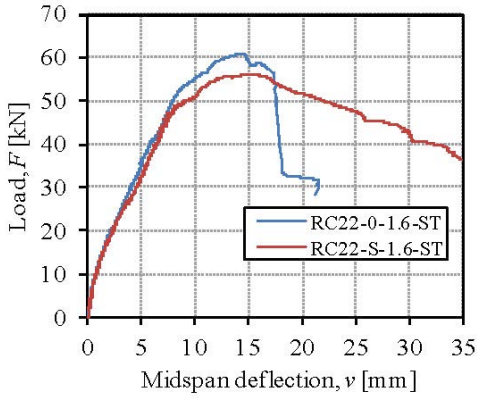


Figure 4. Load-midspan deflection diagrams of quasi-static tests.

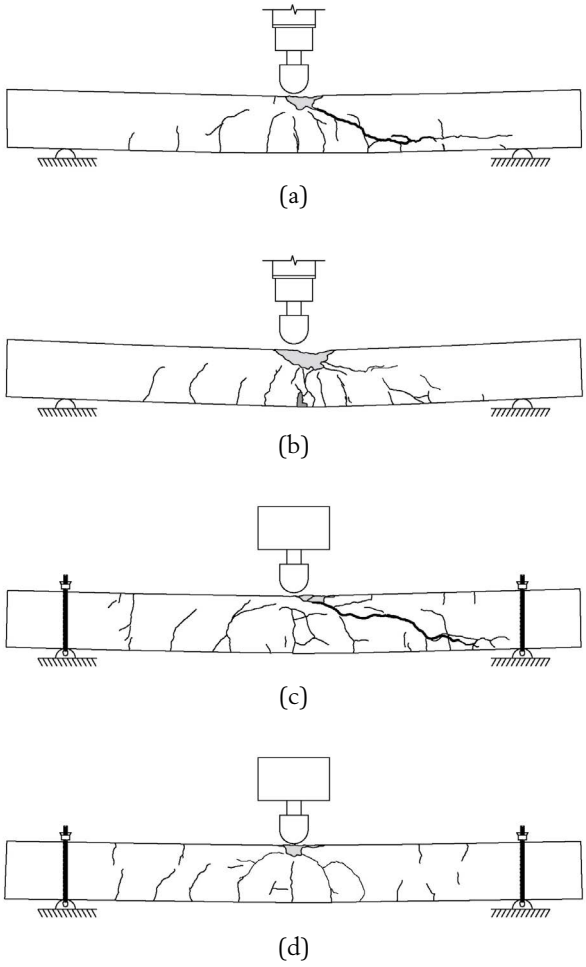


Figure 5. Crack pattern after testing. Quasi-static tests: (a) beam without stirrups, (b) beam with stirrups. Impact tests: (c) beam without stirrups, (d) beam with stirrups.

### 3.2. *Crack pattern evolution in impact tests*

Impact behavior of the tested beams is shown in Figure 6, according to the measurements of the sensors. Both tests had a very impulsive nature, with a high-frequency impact force followed by the development of more moderate reactions, Figure 6(a) and (b). The appearance of the reactions had a delay with respect to the impact force of 2.81 and 2.50 ms, for the beams without and with stirrups, respectively. According to the measurements by the load cells, the six most representative stages of the impact are defined in Figure 6(a) and (b). These stages will be taken as reference to discuss the development of the cracks together with the recorded forces in the following.

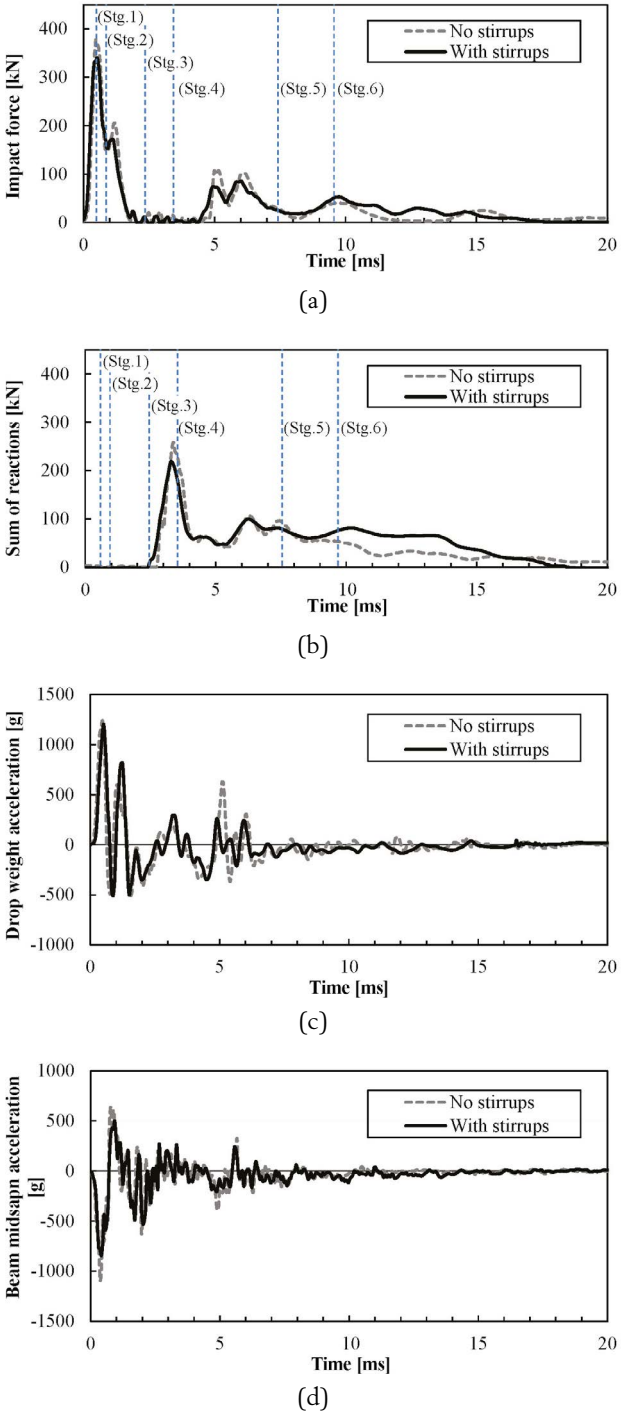


Figure 6. Sensor measurements during the impact loading: (a) falling mass load cell, (b) supports load cells, (c) falling weight accelerometer, (d) beam midspan accelerometer.

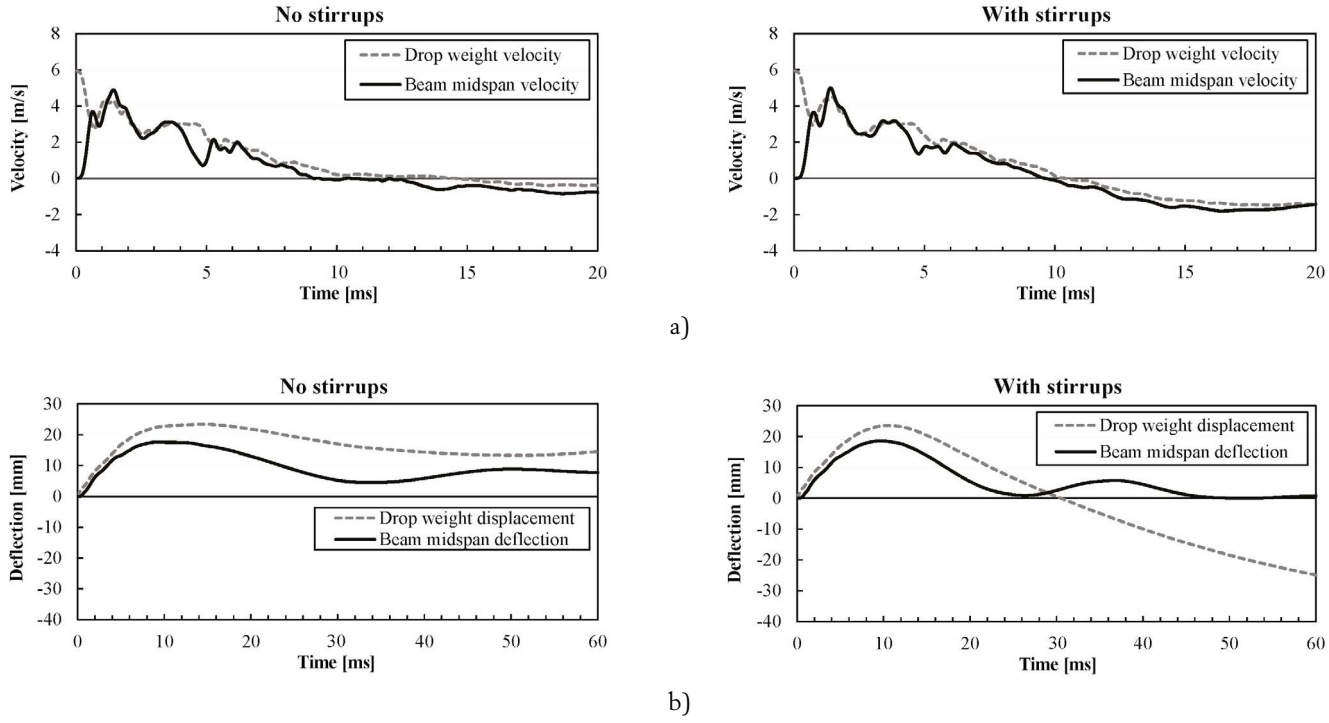


Figure 7. Derived measurements of sensors: (a) velocity and (b) displacements.

The recorded accelerations of the falling mass and the beam at midspan exceeded a peak value of 1000g (Figure 6(c) and (d), respectively). In the first phase of the impact, both accelerations had a contrary tendency. Once the impact force reached its peak, the tendency of both curves was somehow synchronized. The velocity and displacement of the falling mass and beam midspan have been obtained by time integration of the measured accelerations (Figure 7). According to the results, the peak deflection after the impact was similar for both beams (close to 18 mm), while the residual deflection after testing was rather different (a recovery was achieved by the beam with stirrups). In addition, Figure 7 shows that the rebound of the falling mass after the impact was different for each beam, which is an indicator of the energy absorption capacity against the impact. The beam with transverse reinforcement showed a significant rebound of the falling mass, with an upward velocity of 1.5 m/s. Meanwhile, the rebound of the beam without stirrups was smaller, with an upward velocity of 0.56 m/s. This suggests that the energy capacity of the latter beam was seven times smaller than that of the beam with stirrups.

The energy absorption capacity can be correlated with the crack pattern of the beams after impact tests, shown in Figure 5(c) and (d). These images show the formation of a non-critical shear plug and severe flexure cracks close to the impact point at midspan in both beams. In addition, the beam without transverse reinforcement showed a critical diagonal crack running from the midspan to one of the supports, indicating a shear failure mode, while the beam with stirrups only showed non-perfectly vertical bending cracks.

The crack development has been analyzed with the HSV-supported DIC. The results are shown in Figure 8 for the representative stages of the impact, which correspond to the instants marked in Figure 6(a) and (b). The opening of the diagonal cracks is shown in Figure 9, which have been measured with the digital extensometers shown in Figure 2(b). According to these figures, the crack pattern evolution is discussed as follows:

- The first stage (Stg. 1) corresponds to the instant when the impact force reached its peak. Figure 8(a) shows that in this stage there was only a single flexural crack developed in the midspan, below the impact point, at both beams.
- The second stage (Stg. 2) corresponds to the unloading phase of the impact force. Figure 8(b) shows that in this phase there were various flexural cracks at the midspan, being the one formed in previous stage the dominant one, with a wider opening. In addition, a shear-plug developed at both sides of the impact point (detected also with Figure 9). In addition, some negative bending cracks developed from the top face of the beam between the impact point and the supports. Some of these cracks were not perfectly vertical, especially the ones on the right side for the beam without stirrups.
- The third stage (Stg. 3) corresponds to the instant when the reaction forces began, and the impact force had unloaded completely. Figure 8(c) shows that bending cracks in the midspan stabilized and shear plug cracks had fully developed. Though the later cracks were partially hidden behind the drop-weight tower columns (especially in the beam without stirrups), the tip and mouth of these cracks were visible with the camera. In addition, some of the inclined cracks formed during the previous stage (Stg. 2) were still open. Even more, a diagonal crack at the right side of the beam without stirrups (which was later the critical one) started to progress during this stage, accord-

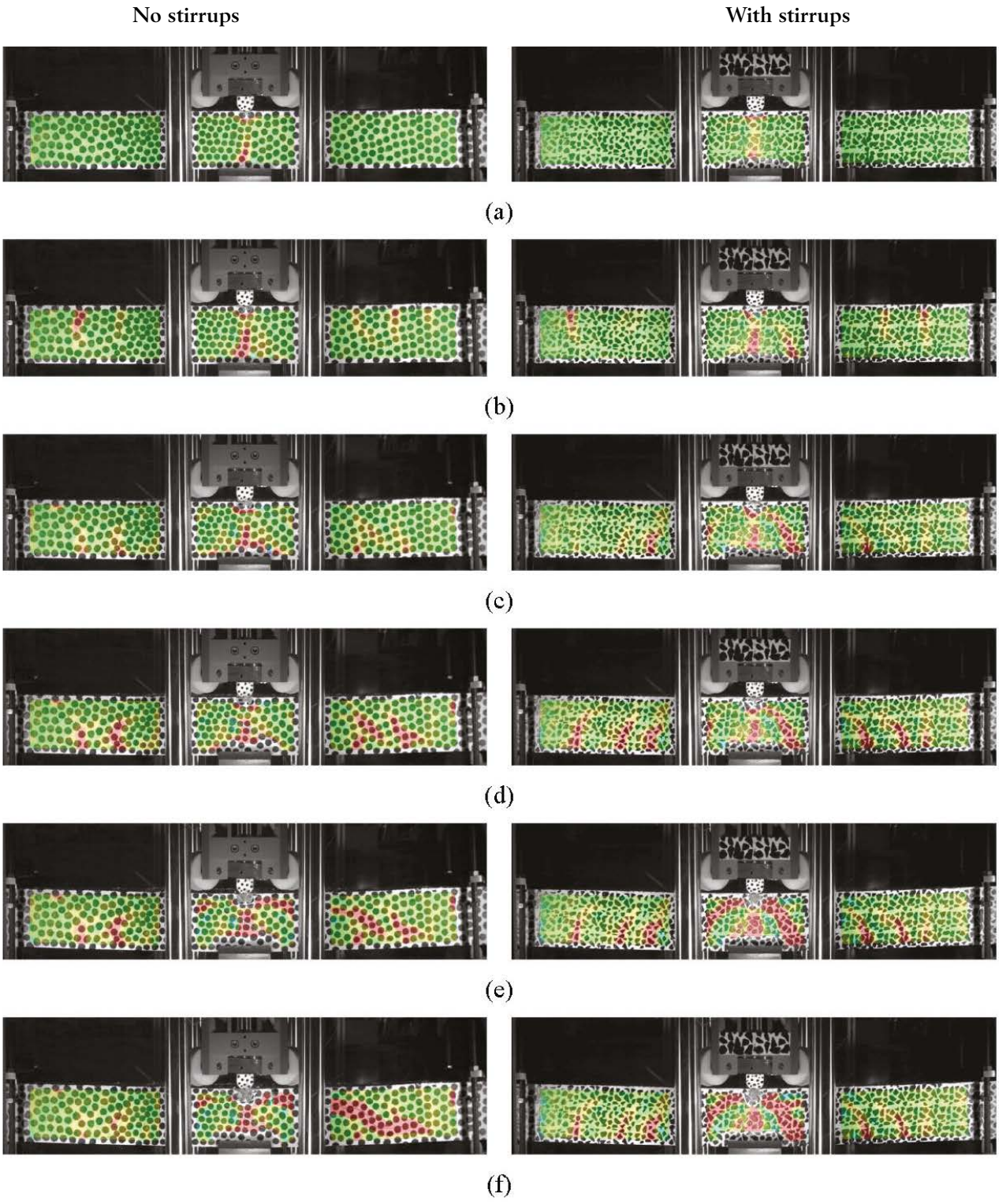


Figure 8. Crack pattern evolution during the impact tests at various stages: (a) Stg. 1, t = 0.49 ms, (b) Stg. 2, t = 0.98 ms, (c) Stg. 3, t = 2.40 ms, (d) Stg. 4, t = 3.42 ms, (e) Stg. 5, t = 7.60 ms, (f) Stg. 6, t = 9.60 ms. Time is defined from the impact beginning.

ing to the measurements of the digital extensometers C3 and C5 shown in Figure 9(a). Below the diagonal cracks new flexural cracks formed from the bottom face of both beams. In the Stg. 3 the distribution of bending cracks seemed to follow the crack pattern of Stg. 2 but with an inverted distribution: most of the existing negative bending cracks closed and some new flexural cracks formed from the bottom (many of them near the sections where negative bending cracks had existed).

- The fourth stage (Stg. 4) corresponds to the peak of the reaction forces. Figure 8(d) shows that existing bending cracks have grown, widened, and inclined towards the loading point. The inclined cracks at the right side of the beam without stirrups stabilized after this stage, Figure 9(a).
- The fifth stage (Stg. 5) is considered just before the total reaction force of the two tested beams started to diverge. Figure 8(e) shows that most of the existing cracks remained stable between Stg. 4 and Stg. 5. A small growth

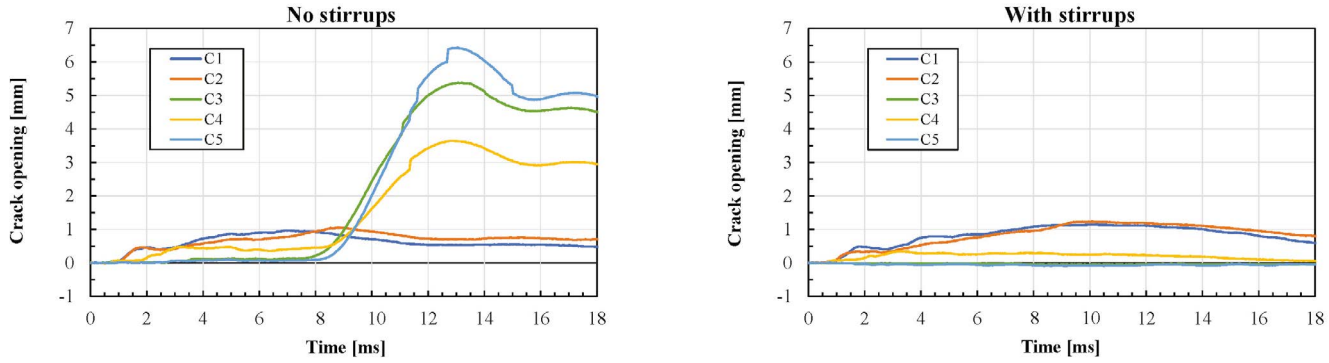


Figure 9. Crack opening from DIC digital extensometers.

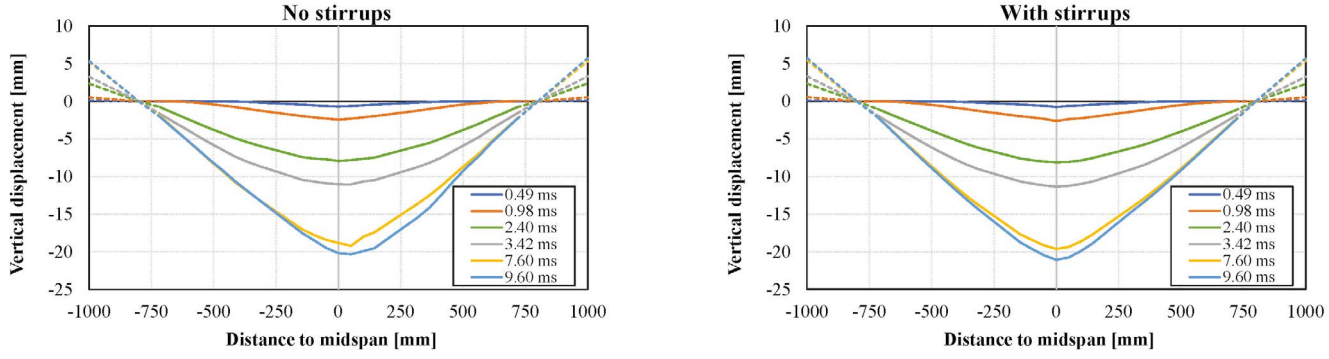


(a)

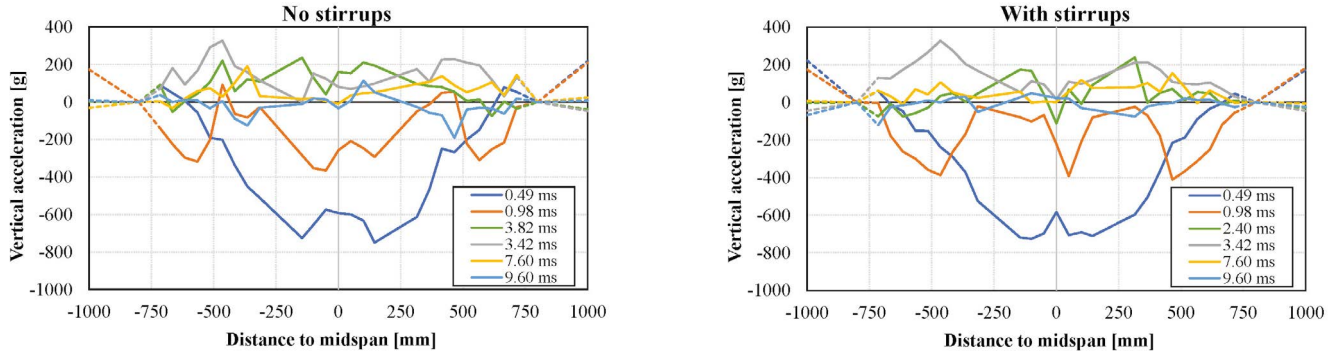


(b)

Figure 10. Parameters distribution and evolution obtained with DIC: (a) deflection, (b) acceleration.

of diagonal cracks on the right side of the beam without stirrups was observed. The only cracks that grew significantly in both beams were the shear plugs (Figure 9).

- The sixth stage (Stg. 6) corresponds to the instant after the divergence of the total reaction force of the beams. This divergence coincides with the different evolution of digital extensometers C3 to C5 at both beams (Figure 9), which might be due to the diagonal crack growth at the right side of the beam without stirrups. Figure 8(f) shows that this crack had fully developed forming a typical shear-bending crack associated with shear failure. The widening of shear-plug cracks stopped at this stage in both beams (Figure 9).

### 3.3. *Extraction of results from DIC*

As explained in Section 2.3, DIC measurements might be employed to obtain the distribution of sectional forces of tested beams. The methodology presented in that Section requires computing the inertia forces from the displacements captured with the DIC. The evolution of the average deflections and accelerations of the tested beams in each cross-section are shown in Figure 10. From the acceleration distribution, the inertia forces have been computed according to Eq. (4). The resultant of inertia forces is compared in Figure 11 with the difference between impact and reaction forces recorded with the load cells (equilibrium according to Eq. 1), which shows that both measurement methods are in excellent agreement. In addition, it might be noted that the different speckle patterns employed (18 and 25 mm) did not have an obvious influence on the results.

From the distribution of inertia forces, the sectional forces of the beams as a function of time can be extracted according to Eq. (2) and (3). However, there are two possible approaches to obtain sectional forces, which differ on how the load-cell forces (impact and support reactions) are considered. In a first approach, the resultant of impact and reaction

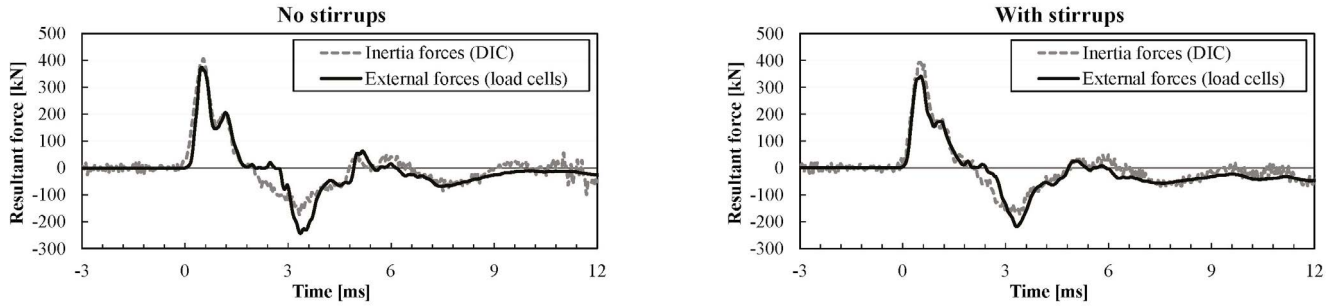


Figure 11. Resultant force for the inertia and external forces. The sign criterion is upwards positive for the inertia forces and negative for the external forces.

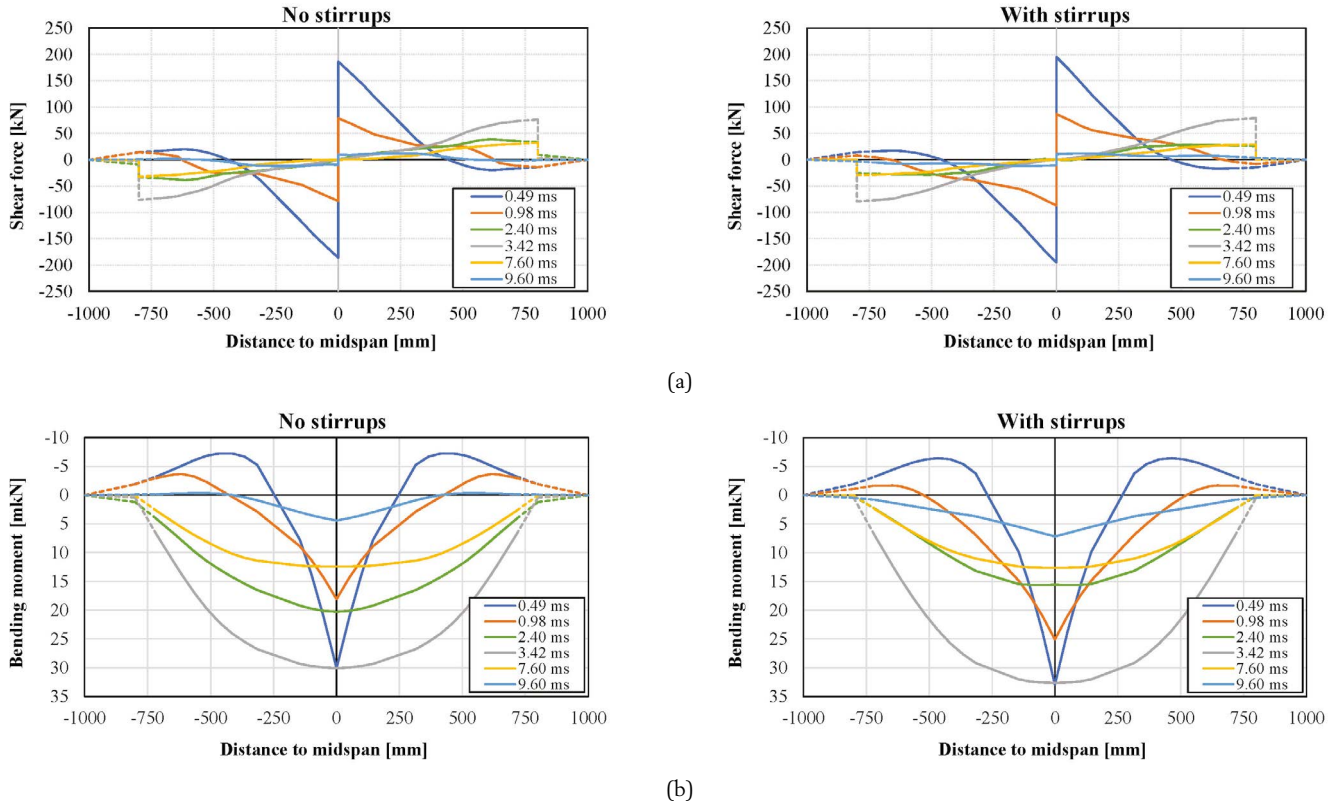


Figure 12. Sectional forces evolution: (a) shear force: (b) bending moment.

forces can be taken as opposite to the inertia forces obtained with the DIC. Such reactions and impact forces can only be positive, upward and downward, respectively. The integration of the reactions and impact forces is done from both beam ends towards the midspan. Meanwhile, in a second approach, the reaction and impact forces can be taken as measured by the load cells. The integration of shear forces in this case is done from the midspan towards the beam ends, considering that the impact force is evenly shared by each side of the beam, taking advantage of symmetry. This integration might lead to non-zero small values of the shear force at the beam ends, which is due to the slight divergences between measured inertia forces and the resultant of reactions and impact forces (Figure 11). The integration of the bending moment in this case must be done considering the effect of the non zero shear force at the ends of the beam. This effect might, in some cases, lead to a non-logical distribution of bending moments. Therefore, the sectional force distributions have been obtained here employing the first approach, considering that the reactions and impact forces are equal and opposite to the inertia forces derived from the DIC.

Sectional forces distributions are shown in Figure 12, for each of the six stages defined in Section 3.2. In the first stages of the impact (before Stg. 3), both the shear and bending moments increased rapidly in the midspan zone, which explains the formation of flexural and shear-plug cracks, see Figure 8(b). The concentration of sectional forces is due to the high value of accelerations at the impacted region in the first stages, Figure 10(b), which produces an upward push of the inertia forces that counteracts the impact effects before reaching the supports. Overtime this concentration is smoothened, due to its propagation. The propagation also has an effect in the observed distribution of bending moments, which shows that initially the beams behave similarly to a fixed-end beam with a variable reduced length over time (which is in agreement with [25,26]). This explains the subsequent formation

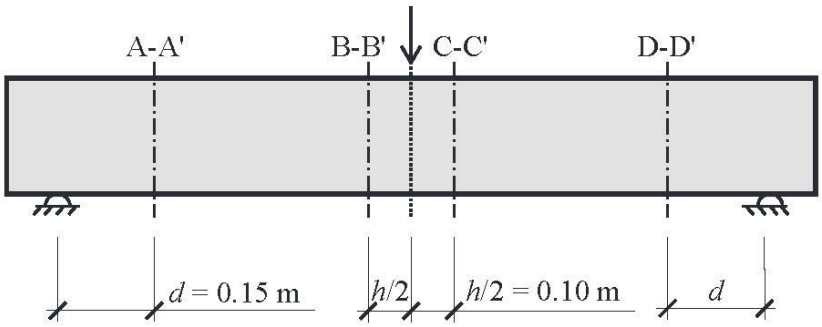


Figure 13. Shear-critical cross-sections in beam specimens.

of negative bending cracks from the top and positive bending cracks from the bottom, as shown in Figure 8(b) and (c).

Once the reactions developed (after Stg. 3), the distribution of sectional forces was somehow similar to that of a simply supported beam under a distributed load, which is consistent with the uneven but relatively uniform distribution of accelerations, Figure 10(b). This stage is characterized by a concentration of shear forces near the supports, and a parabolic distribution of positive bending moments. This distribution suggests a significant shear-bending interaction near the supports in this stage, which is discussed in the following section.

## 4. DISCUSSION OF RESULTS

Two cross-section localizations can be considered critical for shear failure according to the observed crack pattern development, and the typical brittle cracks in impact loading [22,42]. On the one hand, the formation of a local shear plug close to the impact zone can be analyzed at the sections where the shear cracks intersect with the longitudinal axis of the beam. As shear-plug cracks have an inclination of around 45°, the critical cross-sections are those at a distance of h/2 from the midspan (B-B' and C-C' in Figure 13). On the other hand, the development of inclined shear-bending cracks during the global response stage can be analyzed at the cross-sections at a distance d from the supports (A-A' and D-D' in Figure 13), in agreement with common static design rules [11]. Fan *et al.* [40] have adopted similar criteria to define the critical cross-sections, while others [22,23] have mainly focused on the shear-plug cracks.

The strength capacity of each cross-section is governed by the shear-bending interaction. However, existing general models which account for this interaction [8,9,41] have been defined for the quasi-static range. Few proposals exist that focus on this interaction in the dynamic range: Micallef [26] studied the interaction for punching of slabs, while Ulzurrun [42] proposed a model for SFRC beams without stirrups. Both models included the strain-rate effects on the materials properties. In the present study, the shear strength has been computed with the Bentz's simplified version of the Modified Compression Field Theory (SMCFT) [41] for shear strength of reinforced concrete beams. This method is a sectional version of the MCFT [7] which evaluates the shear strength from the stress fields developed in the concrete, considering appropriate equilibrium, compatibility and constitutive equations accounting for stress transfer between crack faces.

In this study the material properties have been modified according to the strain rate and their sensitivity. The formulations considered to obtain the dynamic increase factor (DIF) of the concrete compressive and tensile strength are those defined by [27] and [43], respectively, while for steel yield and ultimate strength is the one proposed by [44]. When dealing with strain-rate effects, it has to be noted that strain rates are variable during the impact event at each point of the structure. Therefore, the material properties should be permanently updated in a time-dependent analysis. Nevertheless, many authors have adopted a simplified approach so that a unique strain rate can be considered sufficient, and typically the maximum has been adopted [34,45]. In turn, Fan *et al.* [40] have shown that variations of the strain rate within the range of 1-10 $s^{-1}$ have small influence and it is acceptable to consider the average value. Other studies [22] have included the strain rate effects as constant in a model based on the general MCFT [7].

The influence of shear-bending interaction in the crack formation at the critical cross-sections is analyzed in Figure 14, which shows the evolution of sectional forces until Stg. 6 ($t$ = 9.4 ms), once the beam without stirrups failed due to the full propagation of a shear-bending crack. The graphics of Figure 14(b) demonstrate that the first stages of the impact tests at sections B-B' and C-C' are governed by a short $M/V$ ratio, or shear slenderness, with an average value of around 0.20 m. Meanwhile, the $M/V$ ratio then increases in the later stages to be approximately equal to the one under a quasi-static distributed loading configuration. Such results, in agreement with [23,34], correspond to the local and global response of the beams, respectively. However, in the study of [34] the global response of the beams was more similar to that of a quasi static point loading configuration. This difference might be explained by more impulsive nature of their tests, with stiffer beams (slenderness $L/h$ = 8, reinforcing ratio of $\rho$ = 1.6 %) and a projectile-to-beam mass ratio 1.92 times higher.

In addition, Figure 14 compares the strength demand (experimental $M$-$V$ evolution) with the theoretical capacity curves, obtained with the Bentz's model at different values of strain rate. These capacity curves represent the envelope of the peak capacity of the beams considering different shear

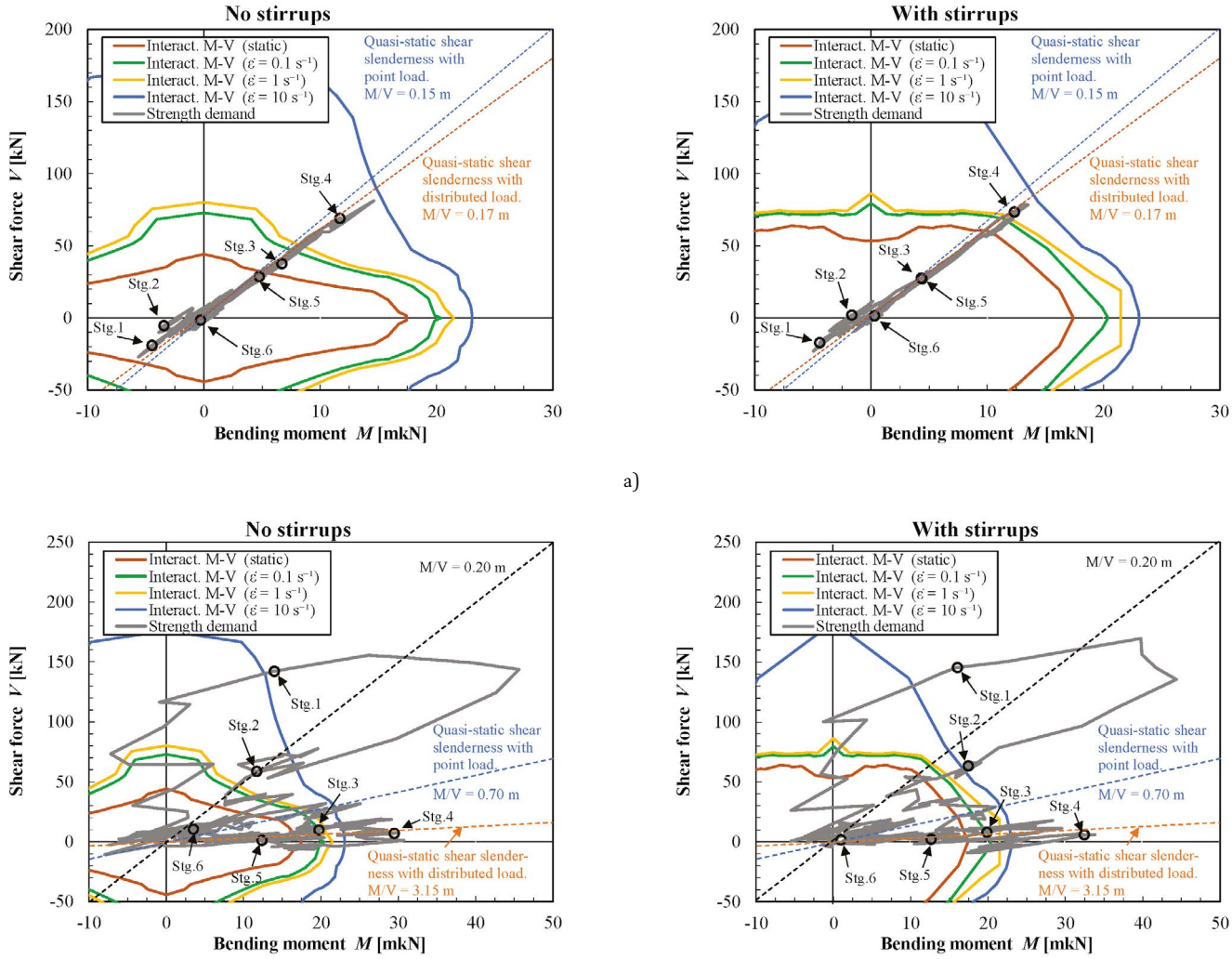


Figure 14. Interaction shear-bending moment in critical sections: (a) section at d = 0.15 m from the supports, A-A' or D-D'; (b) section at h/2 = 0.10 m from the midspan, B B' or C C'.

slenderness (*M/V* ratios). During the first impact stages, the strength capacity was overcome at the midspan sections B-B' and C-C' for both beams, thereby explaining the opening of shear plug within the initial local response of the beams. The strength demand between stages 1 and 2 was even greater than the theoretical beam capacity considering an average strain rate of 10 $s^{-1}$. The shear demand in the sections near the supports (A-A' and D-D') was below the shear capacity in these early stages, but it overpassed the static capacity from stage 3 when the response of the beam shifted from local to global. Furthermore, the dynamic bending capacity was reached at midspan during the global response of the beam, Figure 14(b), which explains the formation of severe flexural cracks in that phase (Figure 8). In the sections near the supports, Figure 14(a), the peak of the shear demand was reached when the M-V evolution laid between the capacity curves corresponding to 1 and 10 $s^{-1}$ at both beams. In the case of the beam without stirrups, the higher demand corresponds to the diagonal crack growth observed during stage 4 (Figure 8 and Figure 9(a)).

According to Figure 14 it is shown that, unlike in a quasi-static test, the shear failure development in an impact test is progressive, reaching the full failure of the beam without stirrups in stage 5, when the *M-V* demand was low, even below the static capacity. The crack propagation velocity can be estimated from Figure 9(a), which yields values ranging from 370 to 620 m/s, of the same order the magnitude as crack propagation velocities reported by other authors in moderate impact regime [47]. It must be reminded that the capacity curves shown in Figure 14 represent the envelope of the peak capacity of the beams. Therefore, they can explain the formation of shear cracks but they do not provide information about the post-peak behavior. There are few models that have included this effect in the dynamic range and the existing ones [26,46] have focused on post-punching behavior. Therefore, it seems convenient to research further on this field in future studies.

## 5. CONCLUSIONS

This manuscript presents the analysis of RC beams under impact loading with the help of HSV-supported DIC in order to determine the time-dependent evolution of shear forces and

bending moments, and its correlation with the crack pattern development. The conclusions obtained from the present research are the following:

- HSV allowed observing the progressive development of bending and shear cracks, with focus on the shear failure development. A shear plug formed during the first local response of tested beams when the effect of the impact force is dominant and the reactions have not yet been activated. In turn, the critical shear-bending crack developed during the global impact response that takes place after the reaction forces have reached their peak.
- The distribution of inertia forces under dynamic impact loading scenarios has a major role in the evolution of sectional forces. The present research shows that these might be assessed by using DIC combined with a HSV camera. By considering the distribution of inertia forces and the evolution of external forces it is possible to evaluate the distribution of sectional forces.
- The distribution of sectional forces at the critical cross-sections compared with the shear-bending capacity curves including strain-rate effects, has allowed discussing the formation shear cracks. Impact tests had two phases as a function of the dominating force, namely the impact or the reactions.
    - The first phase has a very impulsive nature with a high concentration of sectional forces close to the impact point, with significantly large shear forces and an equivalent shear slenderness ratio lower than under quasi-static conditions. The loading conditions in this phase have resulted in the formation of a shear-plug at the midspan of beams with and without stirrups.
    - During the second phase, the distribution of sectional forces is similar to the one caused by a distributed load in quasi-static conditions. This loading pattern has caused the formation of a critical shear-bending crack in the beam without stirrups.

## *Acknowledgements*

The study presented in this paper has received no particular funding, but the experimental infrastructure is a result of previous projects funded by the Spanish research agency (Ref. BIA2012-30998 and BIA2016-74960-R AEI/FEDER, UE).

## *References*

[1] S. Saatci, F.J. Vecchio, Effects of shear resisting mechanisms on impact behavior of reinforced concrete beams, ACI Struct. J. 106 (2009) no. 1 78-86, https://doi.org/10.14359/56286

[2] T.D. Hrynyk, F.J. Vecchio, Behavior of steel fiber-reinforced concrete slabs under impact load, ACI Struct. J. 111 (2014) no. 5 1213-1223, https://doi.org/10.14359/51686923

[3] S.M. Soleimani, N. Banthia, A novel drop weight impact setup for testing reinforced concrete beams, Exp. Tech. 38 (2012) 1-8, https://doi.org/10.1111/j.1747-1567.2012.00810.x

[4] N. Banthia, S. Mindess, A. Bentur, M. Pigeon, Impact testing of concrete using a drop-weight impact machine, Exp. Mech. 29 (1989) 63-69, https://doi.org/10.1007/BF02327783

[5] T. Galkovski, Y. Lemcherreq, J. Mata-Falcón, W. Kaufmann, Fundamental studies on the use of distributed fibre-optical sensing on concrete and reinforcing bars, Sensors 21 (2021) no. 7643 1-24, https://doi.org/10.3390/s21227643

[6] R.C. Elstner, E. Hognestad, Laboratory investigation of rigid frame failure, ACI J. 53 (1957) no. 1 637-668, https://doi.org/10.14359/11540

[7] F.J. Vecchio, M.P. Collins, The modified compression field theory for reinforced concrete elements subjected to shear, ACI J. 83 (1986) no. 2 219-231.

[8] A. Muttoni, M. Fernández Ruiz, Shear strength of members without transverse reinforcement as function of critical shear crack width, ACI Struct. J. 105 (2008) no. 2 163-172, https://doi.org/10.14359/19731

[9] A. Marí, A. Cladera, J. Bairán, E. Oller, C. Ribas, Shear-flexural strength mechanical model for the design and assessment of reinforced concrete beams subjected to point or distributed loads, Fron. Struct. Civil Eng. 8 (2014) no. 4 337-353, https://doi.org/10.1007/s11709-014-0081-0

[10] American Concrete Institute. ACI 318-11: Building Code Requirements for Structural Concrete and Commentary. Framington Hills, MI: American Concrete Institute, 2011.

[11] CEN (European Committee for Normalization). Eurocode 2 EN 1992-1-1:2012. 2012. Design of concrete structures - Part 1: General rules and rules for buildings. Brussels, 2012.

[12] FIB (International Federation for Structural Concrete). Model Code for concrete structures 2010. 2013. Lausanne, Switzerland.

[13] CSA (Canadian Standardization Association). CSA A23.3: 19 Design of concrete structures. 2019. Toronto, ON.

[14] J.M. Gallego, C. Zanuy, L. Albajar, Shear fatigue behaviour of reinforced concrete elements without shear reinforcement, Eng. Struct. 79 (2014) 45-57, https://doi.org/10.1016/j.engstruct.2014.08.005

[15] C. Zanuy, J.M. Gallego, L. Albajar, Fatigue behavior of reinforced concrete haunched beams without stirrups, ACI Struct. J. 112 (2015) no. 3 371-382, https://doi.org/10.14359/51687411

[16] M. Fernández Ruiz, A. Muttoni, J. Sagaseta, Shear strength of concrete members without transverse reinforcement: a mechanical approach to consistently account for size and strain effects, Eng. Struct. 99 (2015) 360-372, https://doi.org/10.1016/j.engstruct.2015.05.007

[17] M. Fernández Ruiz, C. Zanuy, F. Natário, J.M. Gallego, L. Albajar, A. Muttoni, Influence of Fatigue Loading in Shear Failures of Reinforced Concrete Members without Transverse Reinforcement, J. Adv. Concrete Tech. 13 (2015) no. 5 263-274, https://doi.org/10.3151/jact.13.263

[18] G. Ulzurrun, C. Zanuy, Flexural response of SFRC under impact loading, Con. Build. Mat. 134 (2017) 397-411, https://doi.org/10.1016/j.conbuildmat.2016.12.138

[19] G. Ulzurrun, C. Zanuy, Enhancement of impact performance of reinforced concrete beams without stirrups by adding steel fibers, Con. Build. Mat. 145 (2017) 166-182, https://doi.org/10.1016/j.conbuildmat.2017.04.005

[20] S. Saatci, Behaviour and modelling of reinforced concrete structures subjected to impact loads. 2007. PhD thesis. University of Toronto.

[21] K.H. Kishi, H. Mikami, K.G. Matsuoka, T. Ando, Impact behavior of shear-failure type RC beams without shear rebar, Int. J. Impact Eng. 27 (2002) 955-68, https://doi.org/10.1016/S0734-743X(01)00149-X

[22] W.J. Yi, D.B. Zhao, S.K. Kunnath, Simplified approach for assessing shear resistance of reinforced concrete beams under impact loads, ACI Struct. J. 113 (2016) no. 14 747-756, https://doi.org/10.14359/51688617

[23] D.B. Zhao, W.J. Yi, S.K. Kunnath, Numerical simulation and shear resistance of reinforced concrete beams under impact, Eng. Struct. 166 (2018) 387-401, https://doi.org/10.1016/j.engstruct.2018.03.072

[24] D.M. Cotsovos, S.D. Stathopoulos, C.A. Zeris, Behavior of RC beams subjected to high rates of concentrated loading, J. Struct. Eng. 134 (2008) no. 12 1839-1851, https://doi.org/10.1061/(ASCE)0733-9445(2008)134:12(1839)

[25] D.M. Cotsovos, A simplified approach for assessing the load-carrying capacity of reinforced concrete beams under concentrated load applied at high rates, Int. J. Impact Eng. 37 (2010) 907-917, https://doi.org/10.1016/j.ijimpeng.2010.01.005

[26] K. Micallef, J. Sagaseta J, M. Fernández Ruiz M, A. Muttoni, Assessing punching shear failure in reinforced concrete flat slabs subjected to localised impact loading, Int. J. Impact Eng. 71 (2014) 17-33, https://doi.org/10.1016/j.ijimpeng.2014.04.003

[27] CEB-FIP. Model Code for concrete structures. 1991. Lausanne, Switzerland.

[28] N. Madjlessi, D.M. Cotsovos, M. Moatamedi, Drop-weight testing of slender reinforced concrete beams, Struct. Concr. 22 (2021) no. 4 2070-2088, https://doi.org/10.1002/suco.202000395

[29] Spanish Ministry for Transportation, Mobility and Urban Planning. Código Estructural. Vol. III. Dimensionamiento y comporbación de estructuras de hormigón (Spanish code for structural concrete). 2021. Madrid, Spain.

[30] C. Zanuy, G. Ulzurrun, Impact resisting mechanisms of shear-critical reinforced concrete beams strengthened with high-performance FRC, Appl. Sciences 10 (2020) 3154, https://doi.org/10.3390/app10093154

[31] A. Nghiem, T.H.K. Kang, Drop-weight testing on concrete beams and ACI design equations for maximum and residual deflections under low-velocity impact, ACI Struct. J. 117 (2020) no. 2199-210, https://doi.org/10.14359/51721316

[32] GOM. GOM Correlate 2018. Free version. 2018.

[33] J. Leppänen, M. Johansson, P. Grassl, On the dynamic response of reinforced concrete beams subjected to drop weight impact, Finite Elements in Analysis and Design 180 (2020) 103438, https://doi.org/10.1016/j.finel.2020.103438

[34] C. Zanuy, G. Ulzurrun, M. Curbach, Experimental determination of sectional forces in impact tests: application to composite RC-HPFRCC beams, Eng. Struct. 256 (2022) 114004, https://doi.org/10.1016/j.engstruct.2022.114004

[35] M. Johansson, R. Rempling, G. Ulzurrun, C. Zanuy, Key aspects of digital image correlation in impact tests of reinforced concrete beams. IABSE 2019 Symposium Towards a resilient built environment - Risk and asset management. Guimaraes, Portugal. 2019:961-968, https://doi.org/10.2749/guimaraes.2019.0961

[36] M.S. Kirugulige, H.V. Tippur, T.S. Denney, Measurement of transient deformations using digital image correlation method and high-speed photography: application to dynamic fracture, Appl. Opt. 46 (2007) no. 22 1-7, https://doi.org/10.1364/AO.46.005083

[37] M. Hering, F. Bracklow, T. Kühn, M. Curbach, Impact experiments with reinforced concrete plates of different thicknesses, Struct. Concr. 21 (2019) no. 2 587-598, https://doi.org/10.1002/suco.201900195

[38] T. Siebert, T. Becker, K. Splitthof, I. Neumann, R. Krupta, High-speed digital image correlation: error estimations and applications, Opt. Eng. 46 (2007) no. 5 1-7, https://doi.org/10.1117/1.2741217

[39] T. Liu, T.H.K. Kang, A. Nghiem, Y. Xiao, Impact testing of reinforced concrete beams shear-strengthened with fiber-reinforced polymer wraps, ACI Struct. J. 117 (2020) no. 3 297-310, https://doi.org/10.14359/51723497

[40] W. Fan, B. Liu, X. Huang, Y. Sun, Efficient modelling of flexural and shear behaviors in reinforced concrete beams and columns subjected to low-velocity impact loading, Eng. Struct. 195 (2019) 22-50, https://doi.org/ 10.1016/j.engstruct.2019.05.082

[41 E. Bentz, F. Vecchio, M. Collins, Simplified modified compression field theory for calculating shear strength of reinforced concrete elements, ACI Struct. J. 103 (2006) no. 4 614-624, https://doi.org/10.14359/16438

[42] G.S.D. Ulzurrun, Capacidad resistente de elementos lineales de hormigón armado reforzado con fibras bajo cargas de impacto. PhD thesis. Universidad Politécnica de Madrid 2019, https://doi.org/10.20868/UPM.thesis.58074

[43] L.J. Malvar, C.A. Ross, Review of strain rate effects for concrete in tension, ACI Mat. J. 95 (1998) no. 6 735-739, https://doi.org/10.14359/418

[44] L.J. Malvar, Review of static and dynamic properties of steel reinforcing bars, ACI Mat. J. 95 (1998) no. 5 609-616, https://doi.org/10.14359/403

[45] K. Fujikake, B. Li, S. Soeun, Impact response of reinforced concrete beam and its analytical evaluation, J. Struct. Eng. 135 (2009) no. 8 938-950, https://doi.org/10.1061/(ASCE)ST.1943-541X.0000039

[46] CEB (Euro-International Committee for Structural Concrete). Bulletin No. 187. Concrete structures under impact and impulsive loading. Lausanne, Switzerland: CEB, 1988.

[47] M.A. Tarifa Crespo, Procesos de fractura dinámica en hormigón de alta resistencia. PhD thesis. Universidad de Castilla-La Mancha 2012.